PNAS RESEARCH ARTICLE | EARTH, ATMOSPHERIC, AND PLANETARY SCIENCES

Vestiges of impact-driven three-phase mixing in the chemistry and structure of Earth's mantle

Jun Korenaga[a,1] and Simone Marchi[b,1]

Edited by Richard Walker, University of Maryland at College Park, College Park, MD; received May 31, 2023; accepted August 22, 2023

Highly siderophile elements (HSEs; namely Ru, Rh, Pd, Re, Os, Ir, Pt, and Au) in Earth's mantle require the addition of metals after the formation of Earth's core. Early, large collisions have the potential to deliver metals, but the details of their mixing with Earth's mantle remain unresolved. As a large projectile disrupts and penetrates Earth's mantle, a fraction of its metallic core may directly merge with Earth's core. Ensuing gravitational instabilities remove the remaining projectile's core stranded in Earth's mantle, leaving the latter deprived of HSEs. Here, we propose a framework that can efficiently retain the metallic components during large impacts. The mechanism is based on the ubiquitous presence of a partially molten region in the mantle beneath an impact-generated magma ocean, and it involves rapid three-phase flow with solid silicate, molten silicate, and liquid metal as well as long-term mixing by mantle convection. In addition, large low-shear-velocity provinces in the lower mantle may originate from compositional heterogeneities resulting from the proposed three-phase flow during high-energy collisions.

planetary formation | mantle mixing | mantle structure

Significance

Earth's mantle abundance of highly siderophile elements (HSEs), such as gold and platinum, is inexplicably high, given their strong tendency to be contained in its core. This problem has long been thought to be explained by the delivery of HSEs via bombardment of leftover planetesimals. We show that this explanation in its conventional form is geodynamically implausible because of the inability of Earth's mantle to retain the impactor's metals and their HSE budget. However, large impacts can still deliver a sufficient amount of HSEs to the mantle, if we consider the effects of local magma oceans generated by these collisions. We also show that this process provides a natural explanation for the enigmatic seismic structure observed in the present-day Earth's mantle.

Late accretion—the bombardment of leftover planetesimals after the Moon-forming giant impact—has long been thought to explain the observed abundance of highly siderophile elements (HSEs) in Earth's mantle (1, 2). The elevated HSE abundances in the mantle and their chondritic proportions are explained most straightforwardly by the addition of about 0.5% Earth mass of chondritic materials (equivalent to 10^{22} kg of metal) to the mantle after core formation (3, 4). Planetary accretion models as well as asteroidal and lunar constraints suggest, however, that most of late accreted mass is carried by a few large planetesimals with diameters greater than 1,000 km, which are likely to have been differentiated (5, 6). Significant portions of the planetesimals' cores, which contain practically all of HSEs in the planetesimals, could merge with Earth's core, without contributing much to the mantle HSE budget (5, 7). Given this inefficient metal delivery, it has been suggested that the mass of late accretion may be substantially greater than previously thought (up to ~3% Earth mass) to explain the excess HSE abundance in the mantle (5).

A closer look at the metal–silicate distribution resulting from a wide range of smoothed-particle hydrodynamics (SPH) impact simulations indicates that metal retention in the mantle is more difficult than suggested by previous studies (5, 7, 8). Even if a fraction of the impactor's core escapes a direct merger with Earth's core during the simulation of an impact, which usually lasts 24 h or so, it is not likely to contribute to the mantle HSE budget. First, over a wide range of impact conditions, the fragments of the impactor's core found in the solid part of the mantle consist of clumps of several SPH particles (>100 km in diameter), which should sink directly to Earth's core within a few tens of thousands of years (*Methods*). Second, core clumps found in a local magma ocean generated by the impact itself can be further broken up to millimeter- to centimeter-size metal droplets (9, 10). Such droplets are too heavy to be entrained by convection (*Methods*) and quickly settle to the base of the impact-generated magma ocean to form a dense metal layer. The Rayleigh–Taylor instability limits the lifetime of such a metal layer to a day or so (*Methods*), after which the metal sinks to the core even if the mantle below is subsolidus. Finally, gravitationally bound core clumps in orbit are also further broken up to metal droplets (8, 11), but these droplets fall into a local magma ocean, contributing to the metal layer at its base, or onto a solid surface (if any) to form a surface metal layer. Both destinations are subject to the same Rayleigh–Taylor instability (*Methods*). Late accretion thus seems utterly incapable of adding a metallic component to the mantle. Note that the argument here is based on the joint consideration of SPH simulations and laboratory experiments on the efficiency of metal–silicate mixing. We use SPH simulations to capture the initial, highly disruptive and kinematic phases of the

Author affiliations: [a]Department of Earth and Planetary Sciences, Yale University, New Haven, CT 06520; and [b]Department of Space Studies, Southwest Research Institute, Boulder, CO 80302

Author contributions: J.K. and S.M. designed research; performed research; analyzed data; and wrote the paper.

The authors declare no competing interest.

This article is a PNAS Direct Submission.

[1]To whom correspondence may be addressed. Email: jun.korenaga@yale.edu or marchi@boulder.swri.edu.

This article contains supporting information online at https://www.pnas.org/lookup/suppl/doi:10.1073/pnas.2309181120/-/DCSupplemental.

Published October 9, 2023.

projectile–Earth interactions. This approach allows us to assess the large-scale distribution of the projectile's core within Earth. The spatial resolution of SPH simulations is limited to ∼100 km, but finer-scale processes can be deduced from the scaling laws derived from fluid-mechanical experiments (9, 10, 12). One may argue that this suggested inefficiency of retaining a metallic component could be alleviated by redox reactions between metal droplets and silicate melt, but the pressure and temperature dependence of the iron wüstite buffer indicates that the effect of redox reactions on the mantle HSE budget is likely limited (*Methods*). Thus, explaining the excess HSEs by late accretion remains difficult with the existing theoretical framework of geodynamics.

This conundrum, however, may be resolved by the presence of a partially molten zone (a region with a melt fraction less than the critical melt fraction for the rheological transition, i.e., 0.4) beneath both the solid surface and a local magma ocean (Fig. 1). Metal accumulated in a layer can leak into the silicate melt phase in the partially molten zone, and if this process is fast enough, all metal in the layer can be taken up by the partially molten zone (Fig. 2*A*). For large enough impactors ($M/M_e \geq 0.01$), with an optimal impact angle that depends on an impact velocity (usually 45°), the mass of metal that is accessible for this mechanism ("total retained metal" in *SI Appendix*, Fig. S1*C*) can be $\sim 10^{22}$ kg; that is, the subsequent complete mixing of this amount of metal with the mantle can explain the present-day mantle HSE abundances. The partially molten zone itself then becomes gravitationally unstable, and the Rayleigh–Taylor instability brings it down to the base of the mantle within a few tens of thousands of years (Fig. 2*B*; *Methods*). During its descent, however, the silicate melt phase solidifies by adiabatic compression because the mantle solidus increases more sharply than the adiabat with increasing pressures (13, 14). The release of gravitational potential energy heats up the downwelling dense material, but the temperature increase is not sufficient to prevent complete solidification (*Methods*). The adiabatic compression thus successfully traps the metallic phase in the solid mantle. The dynamics of three-phase flow, involving solid silicate, molten silicate, and liquid metal, can thus play a critical role in the aftermath of late accretion impacts.

Results

Metal Percolation Before Rayleigh–Taylor Instability. The speed of downward metal percolation (Fig. 2*A*) is mostly controlled by the permeability of the partially molten zone, which in turn is

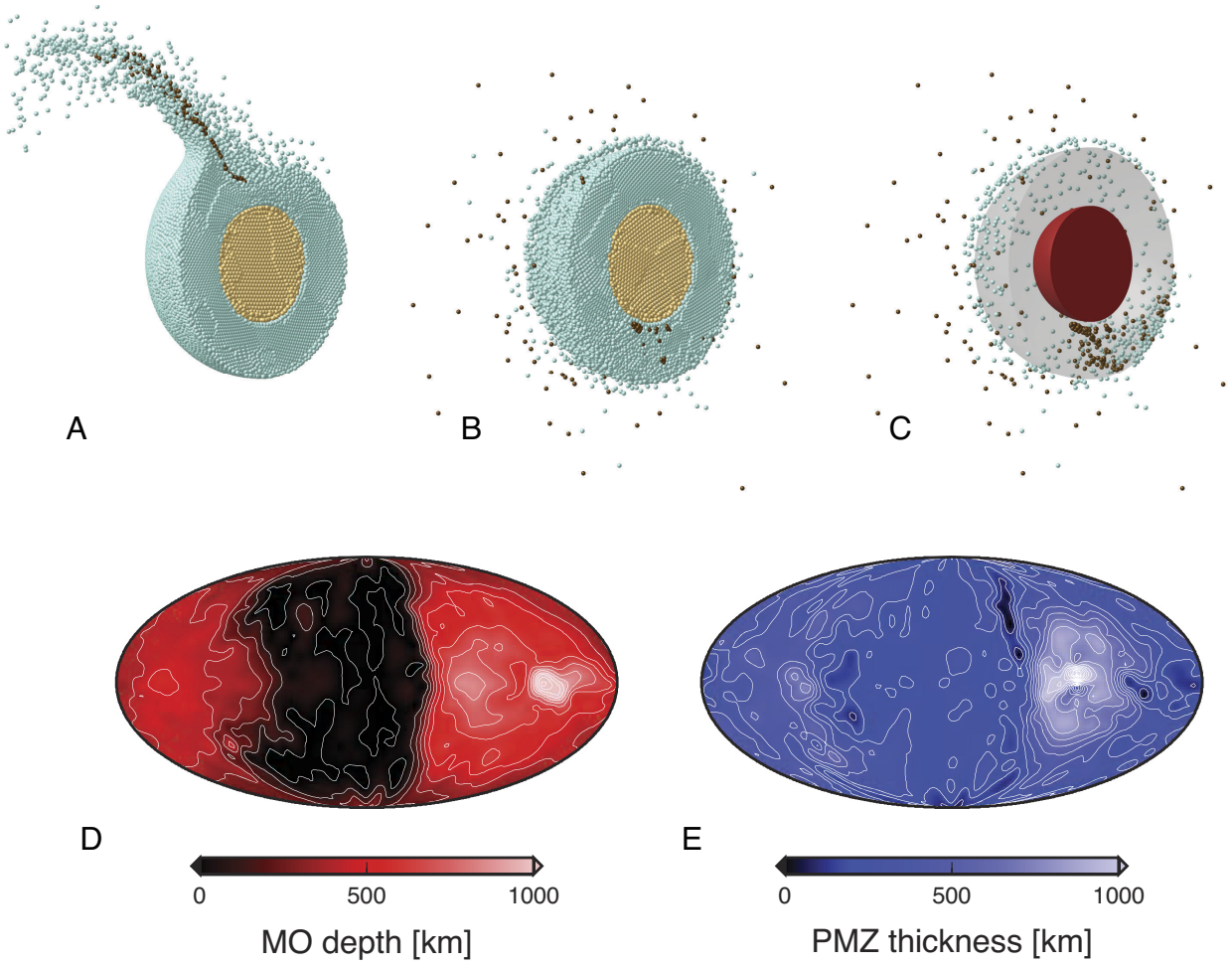

Fig. 1. (*A*–*C*) Representative snapshots of impact simulation for an impactor with 1% Earth mass, an impact velocity of 1.7 times escape velocity (v_e), and an impact angle of 45°. Silicate particles, projectile core particles, and Earth's core particles are, respectively, shown in green, dark brown, and light brown. Panels (*A*) and (*B*) show intermediate (0.3 h after) and final (24 h after) stages of the impact, respectively, and panel (*C*) shows the final stage with projectile particles to better show the 3D distribution of the projectile's core particles (Earth's surface and core are rendered for reference). Also shown are the corresponding distributions of (*D*) magma ocean depth and (*E*) thickness of the partially molten zone. Contours are drawn at an interval of 100 km. Here, magma ocean is defined as regions with melt fraction greater than 0.4.

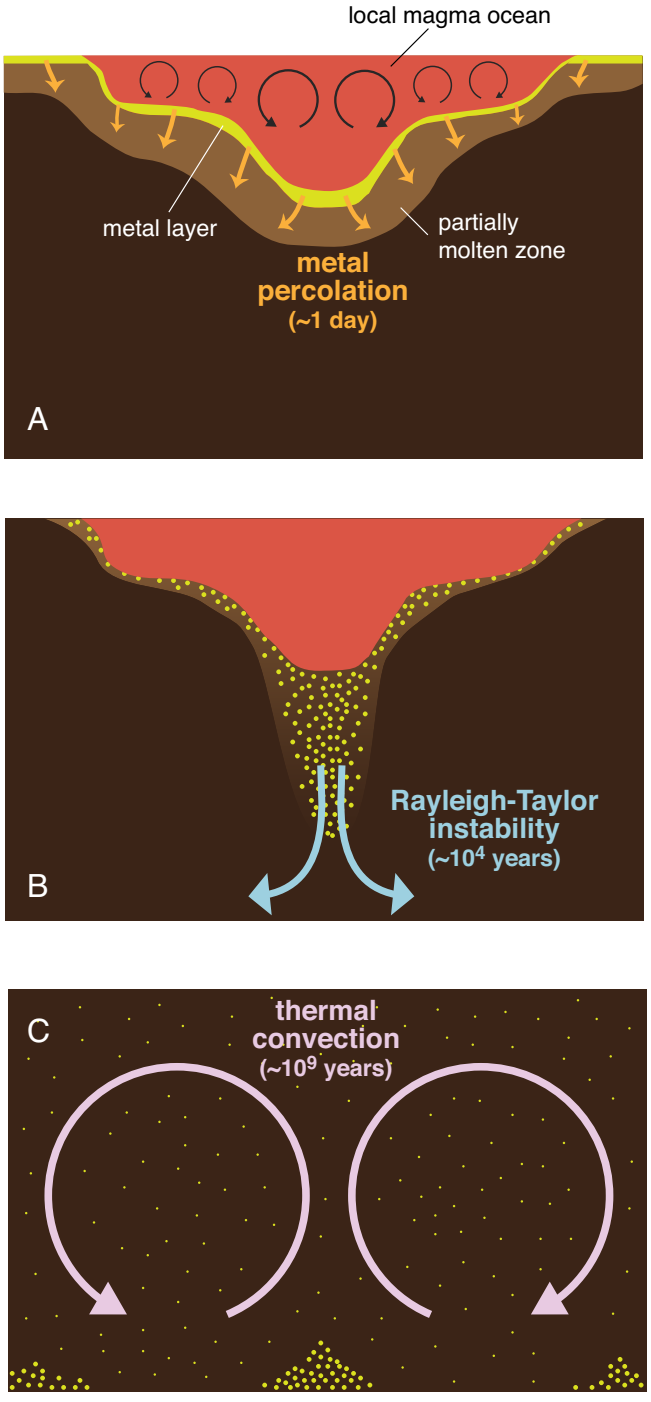

Fig. 2. Schematic illustration for the proposed mechanism of metal retention. (*A*) Metal percolation into the partially molten zone beneath an impact-generated local magma ocean as well as a solid surface. (*B*) Descent of the metal-impregnated partially molten zone by Rayleigh–Taylor instability and its solidification by adiabatic compression. (*C*) Convective mixing of metal-impregnated mantle components above the core–mantle boundary.

sensitive to grain size (*Methods*). Whereas a typical mantle grain size in the present-day mantle is ~1 cm (15), the early mantle is likely to have inherited large grains (up to ~1 m) formed in a solidifying magma ocean where Ostwald ripening is controlled by liquid-state diffusion (16). With a grain size of 10 cm or larger, as much as $\sim 10^{22}$ kg of metal can percolate into the partially molten zone within a day (Fig. 3*A*). Even with the grain size of 1 cm, a similar level of metal percolation can be achieved if the viscosity of the partially molten zone is high enough ($\sim 10^{18}$ Pa s) to lengthen the timescale of the Rayleigh–Taylor instability (*Methods*).

The metal percolation rate of the partially molten zone does not depend on its thickness (Fig. 3*A*), but the thickness matters for the resulting local metal concentration in the zone (Fig. 3*B*). The thickness of a partially molten zone varies substantially among different impacts (*SI Appendix*, Fig. S1*B*), and even for a given impact, it varies across the globe (Fig. 1*C*). Assuming the perfect metal retention by the partially molten zone, local metal fraction can be calculated for the different domains of the mantle, with the one right beneath a locally deep magma ocean persistently having high metal concentrations at a level of ~1 to ~10 wt% (*SI Appendix*, Fig. S1*D*). This is not surprising because such a locally deep magma ocean forms right around the impact site, thereby being likely to contain a substantial fraction of the impactor's core (*SI Appendix*, Tables S1–S3). As discussed below, such regional variability in metal concentration becomes important when considering the fate of metal-impregnated mantle components over Earth history.

Long-term Convective Mixing. After the metal-impregnated partially molten zone is brought down to the core–mantle boundary by the Rayleigh–Taylor instability, the resulting metal-impregnated mantle components can be convectively mixed with

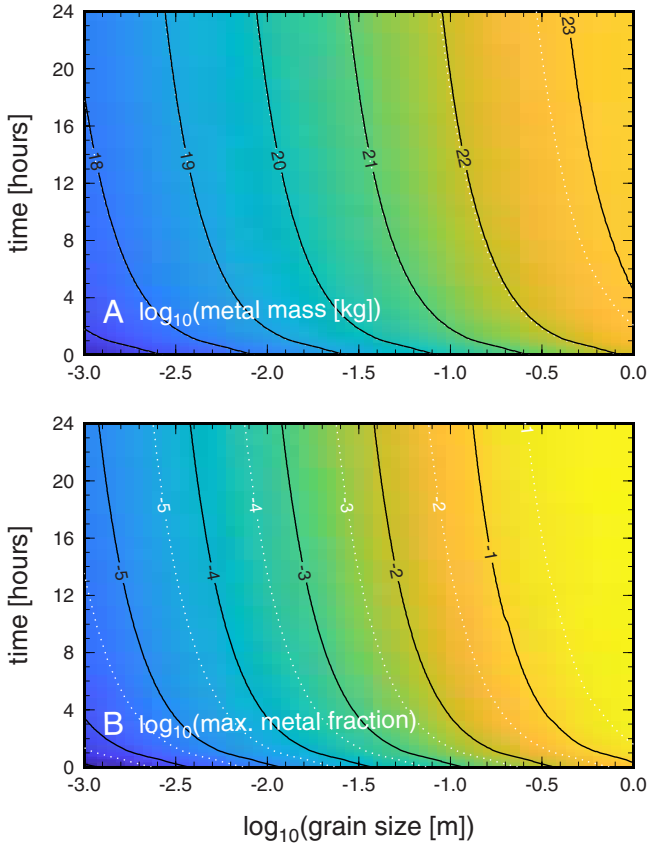

Fig. 3. Metal percolation into a partially molten zone. (*A*) Total mass of metal contained by a partially molten zone and (*B*) maximum metal concentration in the zone, as a function of grain size and time. Metal concentration in a partially molten zone varies with depth, with the maximum concentration at the top of the zone (*SI Appendix*, Fig. S2 *C* and *F*). Black contours are for the case with a 250-km-thick partially molten zone (for which color shading is also shown), and white dot contours are for the case with a 1,000-km-thick zone.

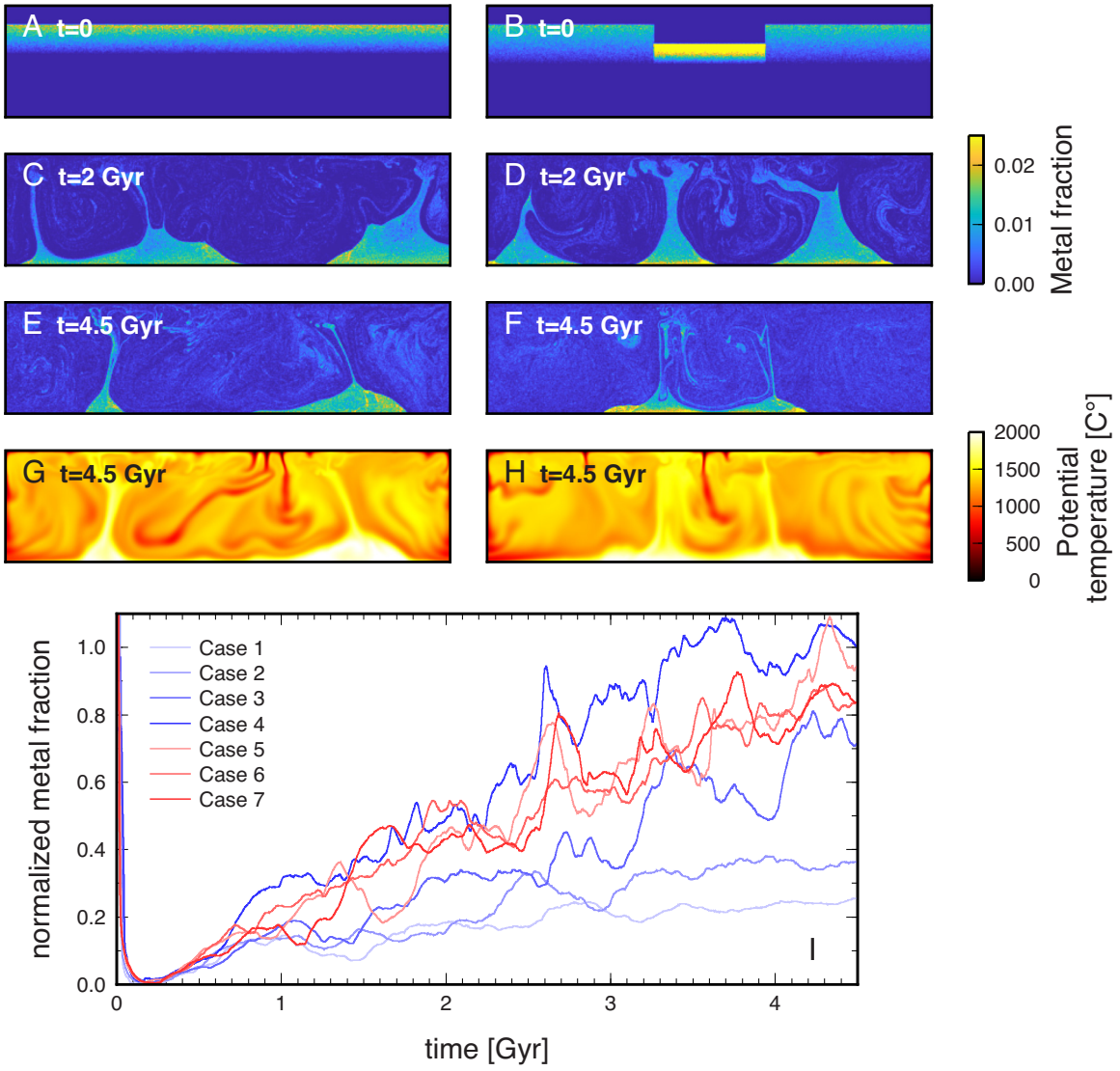

Fig. 4. Some representative results of mixing simulations. Panels (*A*–*F*) show the evolution of the composition field, at three different times: 0, 2 Gyr, and 4.5 Gyr, and (*G*) and (*H*) are the temperature field at 4.5 Gyr. The left column corresponds to case 3 (laterally homogeneous, 750-km-thick partially molten zone with a total metal of 10^{22} kg), and the right column to case 6 (a 1,000-km-thick partially molten zone with a locally deep, more metal-enriched zone, with a total metal of 1.13×10^{22} kg). (*i*) Normalized metal concentration in the top 600 km (1.0 corresponds to the observed present-day level) as a function of time for cases 1–7 (cases 1–4 have laterally homogeneous initial conditions; see *Methods*). All examples shown here are with a Rayleigh number of 3×10^7, nondimensional internal heating of 25, and a Frank–Kamenetskii parameter of 4.61 (see *SI Appendix*, Fig. S3 for other results).

the rest of the mantle (Fig. 2*C*). This mixing is a crucial final step for large impacts to contribute HSEs to the present-day convecting mantle. If some metal-impregnated components are too dense to be entrained by mantle convection, the efficiency of metal delivery would be further reduced. To quantify the effect of mantle mixing, we have conducted a series of mantle convection simulations by exploring a range of initial conditions, mantle rheology, and mantle thermal budget (*Methods*). Some representative results are shown in Fig. 4. If metal concentrations in the metal-impregnated zone are sufficiently low ($\lesssim$1 wt%), it is possible to entrain all of metal-impregnated components within a few billion years. Such low concentrations may be achieved by either a thick partially molten zone or a low metal mass. However, the thickness of the partially molten zone and its metal concentration are positively correlated; with an increasing impactor size, both the thickness of the partially molten zone and the total mass of retained metal increase, but the former increases more weakly than the latter. Thus, a low concentration usually corresponds to a metal mass much smaller than the required 10^{22} kg for the whole mantle (*SI Appendix*, Fig. S1*D*). Furthermore, as noted above, the occurrence of regionally high metal concentrations is the robust aspect of the aftermath of late accretion impacts (*SI Appendix*, Fig. S1*D*), and it is difficult to avoid having denser metal-impregnated components (i.e., $\gtrsim$1 wt% metal concentration) at the base of the mantle that can survive convective mixing throughout Earth history (Fig. 4). Uncertainties associated with mantle rheology (17, 18) prevent us from being specific about the mixing efficiency of mantle convection, but an efficiency of 100% (i.e., complete mixing) certainly requires fortuitous combinations of initial conditions and mantle rheology. We also note that the density requirement for the survival of the metal-impregnated components ($\sim$1%) varies with the assumption of mantle rheology, and a lower threshold may be more appropriate given the use of relatively high reference viscosity in our convection modeling (*Methods*).

Discussion

Implications for Mantle Structure and Evolution. A high likelihood for incomplete mantle mixing has important implications for the present-day mantle structure as well as the chemical evolution of the mantle. The lowermost part of Earth's mantle exhibits peculiar seismic anomalies known as large low-shear-velocity provinces (LLSVPs) (19, 20), the origin of which is actively debated. One end-member explanation posits LLSVPs, or more generally, deep-mantle chemical heterogeneities, as the remnants of a primordial structure formed by some early Earth differentiation processes (21–23), with some involving the Moon-forming giant impact (24, 25). Unlike existing impact-based hypotheses for such primordial origins, the possibility raised in this study, i.e., incomplete mixing of metal delivered by late accretion, does not require a large preexisting compositional difference (in terms of major elements) between the proto-Earth and an impactor. The total mass of LLSVPs has been estimated to be ~4–9% of the mantle (26), and with an intrinsic density anomaly of ~0.5% (27–29), LLSVPs could contain ~1–2×10^{21} kg of metals. Because the present-day convecting mantle itself contains ~10^{22} kg of metals, a mixing efficiency of ~80–90% could explain the formation of LLSVPs, with the total metal delivery of ~1.1–1.2 $\times10^{22}$ kg. This level of metal delivery is possible with an impactor with 3% Earth mass, an impact angle of 45°, and an impact velocity of either $1.2v_e$ or $1.7v_e$, where v_e denotes escape velocity (*SI Appendix*, Tables S1–S3). It is also possible to deliver a similar amount of metal by a combination of a few differentiated lunar-sized impactors (about 0.01 M_e), or more numerous smaller impactors (down to 0.001 M_e), and the plausibility of different scenarios depends on the impactor size-frequency distribution for the early Earth.

Our hypothesis for the primordial origin of LLSVPs also indicates that the mantle HSE budget should have gradually increased with a timescale of a few billion years (Fig. 4, *i*), and such a gradual increase in the mantle HSE budget is indeed indicated by geochemical data (30–32). For example, adding 10^{22} kg of core materials to the mantle would decrease the mantle μ^{182}W [defined as $[(^{182}W/^{184}W)_{sample}-(^{182}W/^{184}W)_{standard}]\times10^6$] by about 18 [assuming the core W concentration of 0.47 ppm (33), the mantle W concentration of 12 ppb (34), and the core μ^{182}W of −220 (35)], and this level of μ^{182}W variation is consistent with the observed secular evolution of the mantle μ^{182}W (32). We caution that it is difficult to accurately estimate the HSE concentration of the convecting mantle from igneous products (36) and that there is no clear correlation between the HSE abundances of igneous products and their tungsten isotope signatures (32). The lack of correlation between HSE abundances and tungsten isotope signatures is particularly concerning because such a correlation is expected from simple mixing of metal-impregnated components. However, the tungsten isotope signature of the mantle can also be affected by diffusional isotope exchange with the core (i.e., without the net mass transfer of tungsten from the core) (37, 38). If such an isotope exchange with the core is as important as convective mixing within the mantle, the lack of correlation would not pose a serious impediment to our hypothesis.

The above connection between late accretion and LLSVPs provides some observational means to test our hypothesis, which posits that LLSVPs are characterized by intrinsic density anomalies originating in the addition of metallic components of late accretion impactors. The magnitude of intrinsic density anomalies associated with LLSVPs is still poorly constrained (29), but a refined estimate on the total mass anomaly associated with LLSVPs will allow a more critical assessment of the late accretion origin. As mentioned above, diffusional isotope exchange with the core could blur the geochemical signature of the late accretion origin of LLSVPs, but diffusional exchange is not limited to tungsten isotopes. One of the useful isotope systems in this regard is the U-Th-Pb system, which is contrasting to the ^{182}Hf-^{182}W system in both half-life and the direction of diffusion. As the ^{182}Hf-^{182}W system is short-lived with a half-life of 8.9 million years, diffusional exchange at the core–mantle boundary results in the leaking of a strongly negative μ^{182}W anomaly out of the core. The U-Th-Pb system is characterized by much longer half-lives (e.g., 4.47 billion years for ^{238}U-^{206}Pb), so diffusional exchange results in the net flow of radiogenic Pb isotopes into the core, and such flow is affected by the long-term evolution of U and Th in the mantle. Thus, combining these different isotope systems could better quantify the extent of diffusional exchange. Indeed, the tungsten isotope signatures of ocean island basalts show some slight variations with lead isotopes (39), so more extensive studies of ocean island basalt geochemistry, along with suitable modeling efforts, may ultimately judge the viability of the late accretion origin of LLSVPs.

Potential Role of the Moon-forming Giant Impact. The possibility of incomplete mantle mixing suggests that, to explain the excess HSEs of the present-day convecting mantle, the total mass of late accretion is close to the upper limit of previous estimates (~3% Earth mass). Some fraction of the excess HSEs may originate from other processes not involving late accretion, and indeed, metal retention by a partially molten zone beneath a magma ocean is not limited to late accretion. It could also happen in the aftermath of the Moon-forming giant impact if the impact does not melt the entire mantle (40). The possibility of metal retention in the mantle during the Moon-forming giant impact has been suggested in the past (41, 42), but this possibility requires the oxidation of metal droplets in a magma ocean (42), which is unlikely to be substantial (*Methods*). Metal retention by three-phase flow is an entirely different physical mechanism. For this mechanism to work, however, an impact must not melt the entire mantle—a partially molten zone has to be underlain by the solid mantle to prevent metal percolation directly down to the core, and the solid mantle layer must be sufficiently thick so that adiabatic compression during Rayleigh–Taylor instability can solidify silicate melt. Satisfying these conditions is easy for late accretion impacts but may be challenging for the Moon-forming giant impact.

Summary

Adding HSEs in chondritic proportions can readily be achieved by mixing the metallic components of planetesimals with the mantle, but such mixing is seemingly unlikely because of the sheer magnitude of gravitational instability associated with such metallic components. The solution proposed in this study is based on the existence of a partially molten zone beneath an impact-generated magma ocean, which should always exist unless a magma ocean occupies the entire mantle. As this study suggests, metal percolation into such a partially molten zone, through three-phase flow, may be essential to explain the chemical composition of the present-day convecting mantle. A cascade of processes follow this metal percolation, including the downwelling of the metal-impregnated partially molten zone by the Rayleigh–Taylor instability, the entrapment of the metal

phase by the compressional solidification of the silicate melt phase, and the subsequent entrainment of the metal-impregnated components at the core–mantle boundary by convective mixing. The first two processes take place rapidly within a few tens of thousands of years, but the third mixing process is likely to be still ongoing, which can be connected to peculiar geophysical features in the present-day deep mantle. This study provides a concrete and quantitative mechanism for the primordial origin of large low-shear-velocity provinces in Earth's lower mantle, as the natural consequence of combining (short-term) impact dynamics and (long-term) mantle dynamics. We suggest that three-phase flow in the aftermath of high-energy accretionary impacts is an essential process that bridges early Earth geodynamics and the present-day physical and chemical state of the mantle.

Methods

Postprocessing of SPH Simulations. SPH impact simulations used in ref. 5 are postprocessed to characterize the extent of impact-generated magma oceans and their relation to the spatial distribution of the impactor's metallic components. To this end, for each SPH simulation, a suitable time step for postprocessing is chosen to avoid the initial phase of impact-generated high-amplitude and high-frequency deformation. The time step is chosen to be as early as possible after impact once the phase of major disruption of Earth has settled. This highly dynamic phase requires the use of the SPH method to fully account for shock and gravitational effects. This phase is concluded typically within a few hours after impact. This choice is motivated by our attempt to limit the subsequent migration of projectile's metal particles which is not well captured by the SPH technique. As the SPH simulations of ref. 5 take into account the effect of solid–solid phase transitions, but not that of latent heat of melting, the thermal structure of the target (i.e., the impacted Earth) at the chosen time step is compared with the initial thermal structure, and the temperature difference is used to calculate the extent of mantle melting using the phase diagram of the peridotitic mantle (13, 14, 43, 44). Regions with a melt fraction greater than 0.4 are marked as "molten"; this melt fraction is often regarded as the critical melt fraction for the rheological transition, above which a melt-solid mixture behaves as liquid (45, 46). Regions with nonzero melt fraction below 0.4 are marked as "partially molten." The surface is divided into ∼600 grids with approximately equal areas, and Earth is partitioned by using the solid angles of these grids. For each grid, the depth of a magma ocean and the thickness of a partially molten zone beneath it are measured. The spatial variability of magma ocean depth is characterized by its first quartile (Q_1), the median (Q_2), and the third quartile (Q_3), and a region with magma ocean depths exceeding Q_3 is defined as a locally deep magma ocean.

The particles of the impactor's core are 1) ejected and gravitationally unbound, 2) ejected and gravitationally bound, 3) directly merged with the core or the solid part of the mantle, and 4) in the magma ocean. We also measure the total mass of core particles found in the locally deep magma ocean. The ejected and gravitationally bound particles eventually fall back onto Earth, and they are assumed to contribute to the magma ocean and the unmolten surface in proportion to their areas. The spatial distribution of the core particles found in the magma ocean and the solid part of the mantle is analyzed by agglomerative hierarchical clustering (47), using the effective diameter of the core particle as the threshold for linkage. The results of postprocessing are summarized in *SI Appendix*, Tables S1–S3.

Time Scale Estimates.

Stokes flow for metallic fragments. SPH impact simulations show that a large fraction of an impactor's core directly plunges into the core or into the solid part of the mantle (5) (listed as "direct" in *SI Appendix*, Tables S1–S3). The part that plunges into the solid mantle is treated as retained metal by the original study of ref. 5, but such metal fragments are usually of large dimension with diameters typically greater than a few hundred kilometers. Only for the cases with an impactor mass of 3% Earth, a large fraction of core particles found in the solid part of the mantle exists as single particles (see n_{SM} in *SI Appendix*, Tables S1–S3), and in reality, these single core particles could have been more fragmented, which is the possibility that cannot be resolved by SPH simulations. A representative estimate on the downwelling speed of such fragments through the mantle may be obtained by using the size of individual particles in SPH simulations, and for the simulations analyzed in this study, the effective radius of core particles, which was calculated from the particle mass and metal density of 7,800 kg m^{-3}, was for ∼90 km for impactors with their masses greater than 0.1% Earth and ∼50 km for smaller impactors. The descent velocity of a spherical body in a viscous fluid is given by the following Stokes flow formula (48):

$$v = \frac{2\Delta\rho g r^2}{9\mu}, \quad [1]$$

where $\Delta\rho$ is the density difference between a metallic sphere and the surrounding mantle, g is the gravitational acceleration, r is the radius of the sphere, and μ is the viscosity of the mantle. As a consequence of impact heating, most of these core particles are found within the partially molten zone, so the relevant mantle viscosity for their descent is very low, on the order of 10^{16}–10^{19} Pa s (14). With a mantle viscosity of 10^{19} Pa s and a density difference of 4,000 kg m^{-3}, for example, a metallic sphere with a radius of 50 km, would sink with a velocity of ∼70 m y^{-1}. Thus, those large metallic fragments (i.e., multiple-particle clusters) that remain in the solid part of the mantle at the end of SPH simulation (24 h after impact) will likely merge with the core within a few tens of thousands of years. The fate of single core particles needs further consideration, as they could have been further fragmented, and the Stokes flow formula indicates that the time scale increases by two orders of magnitude for a one-order-of-magnitude decrease in the radius of fragments. Continuing with a mantle viscosity of 10^{19} Pa s [a typical solid mantle viscosity for a hot Hadean mantle (49)], a metallic sphere with a radius of 1 km will take about 100 My to sink through the entire mantle, so fragmentation down to this length scale may allow its retainment within the mantle. Even with such fragmentation, however, the contribution of such single core particles to the HSE budget of the mantle is limited. To account for a total mass of 10^{22} kg, for example, the number of core particles needs to be ∼440, and except for only one case of a 3% Earth mass impactor with head-on collision and $v/v_e = 2.2$, single core particles found in the solid part of the mantle can account for up to only $\sim 1.5 \times 10^{21}$ kg (*SI Appendix*, Tables S1–S3). Furthermore, these fragmented metallic components, unless broken down to submeter scales, would be too dense to be entrained by mantle convection, and they would most likely descend through the mantle and eventually merge with the core.

Rayleigh–Taylor instability of a metal layer. The metallic components found in an impact-generated magma ocean exist mostly as single core particles (see n_{MO} in *SI Appendix*, Tables S1–S3), and they are likely to be fragmented, possibly down to millimeter- to centimeter-sized droplets (9, 10), before they reach the base of the magma ocean. Even if they are too large to be fragmented so finely before reaching the base, crashing into the base would result in further fragmentation by turbulent mixing (9). Because of their density, however, these metallic droplets cannot be entrained efficiently even by vigorous convection within the magma ocean. The fraction of entrained metallic droplets may be estimated based on the scaling developed by ref. 12:

$$\xi = \epsilon \frac{9\pi^2}{2} \frac{\kappa^2 \nu_a \nu}{H^4 g^2 R^2} \left(\frac{Ra}{Ra_c}\right)^{4/3} \left(\frac{\Delta\rho}{\rho}\right)^{-2}, \quad [2]$$

where ϵ is a scaling factor (= 0.25), κ is thermal diffusivity (= 10^{-6} m^2 s^{-1}), ρ is the density of silicate melt (= 3,000 kg m^{-3}), $\Delta\rho$ is the excess density for metal particle (= 4,000 kg m^{-3}), Ra_c is the critical Rayleigh number (= 10^3), H is the thickness of a magma ocean (∼10^6 m), R is the radius of the metallic droplets (= 10^{-3} m), ν is the kinematic viscosity of silicate melt (= η/ρ, where η is the dynamic viscosity, which is set to 0.1 Pa s), ν_a is the apparent kinematic viscosity defined as $\nu(Ra/Ra_c)^{0.06}$, and Ra is the Rayleigh number defined as

$$Ra = \frac{\alpha g \Delta T H^3}{\nu\kappa}, \quad [3]$$

where α is thermal expansivity ($= 2 \times 10^{-5}$ K^{-1}), ΔT is the temperature difference driving convection. Using these material properties, the fraction ξ is found to be $\sim 10^{-6}$, meaning that virtually all metallic droplets must accumulate as a layer above the base of the magma ocean. The thickness of such a metallic layer is on the order of a few hundred meters to a few kilometers (*SI Appendix*, Tables S1–S3). For example, for the case of a 1% Earth mass impactor with an impact angle of 45° and $v/v_e = 1.7$, 9.3 wt% of the impactor's core is found in the local magma ocean, which covers 54% of the total surface. Because 36.7 wt% of the impactor's core is in the vacuum and gravitationally bound, additional 19.8 wt% of the core materials will fall into the magma ocean. With a metal density of 7,800 kg m^{-3}, this translates to a ~3-km-thick metallic layer at the bottom of the local magma ocean. At the same time, 16.9 wt% of the core materials will fall onto the solid part of the surface (i.e., melt fraction less than 0.4), resulting in a ~1.8-km-thick metallic layer. The Rayleigh–Taylor instability of these metallic layers, for which the effects of inertia and self-gravity are important, can be assessed by the empirical scaling developed by ref. 50:

$$\sigma = 10^{-10.13} R_1^{1.86} (\rho_2 - \rho_1)^{1.3} \rho_1^{0.87} (R_2 - R_1)^{0.047} \mu_1^{-0.98} \mu_2^{-0.054}, \quad [4]$$

where σ is the growth rate of the instability in the unit of s^{-1}, R_1 is the radius of the solid sphere underlying the magma ocean, R_2 is the radius of the sphere including the magma ocean, ρ_1 and ρ_2 are the densities of the solid mantle and the metallic components, respectively, and μ_1 and μ_2 are their corresponding viscosities. Using representative values ($R_1 \sim 5 \times 10^6$ m, $R_2 - R_1 \sim 10^3$ m, $\rho_1 \sim 4{,}000$ kg m^{-3}, $\rho_2 - \rho_1 \sim 4{,}000$ kg m^{-3}, $\mu_1 \sim 10^{15}$ Pa s, and $\mu_2 \sim 10^{-3}$ Pa s), the growth rate is on the order of 10^{-4} s^{-1}, that is, the *e*-folding timescale of the instability is a few hours. Note that this time scale is not very sensitive to the thickness of the metallic layer as indicated by the low thickness exponent (i.e., 0.047) in the above equation. Given that it takes a multiple of *e*-folding timescale for initial minute perturbations to grow into large-scale deformation, it would be reasonable to assume that a metallic layer will be fully destabilized within a day or so. The viscosity of the solid mantle beneath the metallic layer assumed here (~10^{15} Pa s) corresponds to the viscosity of the solid-melt mixture at the rheological transition (14), which is most relevant for the Rayleigh–Taylor instability under consideration. A higher viscosity would increase the timescale of instability almost linearly, helping metal percolation into the partially molten zone. By reducing the melt fraction from 0.4 to 0.1, for example, viscosity increases by three orders of magnitude (14), thereby lengthening the destabilization timescale to a few years. Such a time scale would allow complete metal percolation even with a grain size of 1 cm.

Rayleigh–Taylor instability of a metal-impregnated partially molten mantle layer. A partially molten zone that has taken up the overlying metallic layer eventually becomes gravitationally unstable because the silicate melt phase, if buoyant, drains upward continuously by melt percolation. The melt phase is not necessarily buoyant with respect to the solid phase at high pressures (51), and in such a case, metal percolation alone would make the partially molten zone gravitationally unstable. Unlike the instability of the purely metallic layer, the effect of inertia can be neglected because the viscosity of the metal-impregnated zone is high enough. Based on the analysis of the low-Reynolds-number dynamics of a thin fluid layer (52), therefore, the growth rate of the Rayleigh–Taylor instability may be estimated as

$$\sigma = 0.149 \frac{g \Delta \rho h}{\mu_m}, \quad [5]$$

where $\Delta\rho$ is the density contrast (~40 kg m^{-3}; *SI Appendix*, Fig. S1*D*), h is the thickness of the partially molten zone (~5×10^5 m; *SI Appendix*, Fig. S1*B*), and μ_m is the viscosity of the mantle beneath the partially molten zone (e.g., ~ 10^{19} Pa s). The growth rate is on the order of 10^{-11} s^{-1}, so the metal-impregnated mantle layer is destabilized within a few tens of thousands of years.

Heating by Gravitational Potential Energy Release. When the metal-impregnated partially molten zone sinks to the core–mantle boundary by the Rayleigh–Taylor instability, its temperature increases not only by adiabatic compression, but also by the release of gravitational potential energy because the partially molten zone is intrinsically denser than the surrounding mantle. An upper bound on the latter temperature increase can be obtained by dividing the energy release by the relevant heat capacity as

$$\Delta T = \frac{\Delta \rho \Delta V g d}{\rho \Delta V C_p}, \quad [6]$$

where $\Delta\rho$ is the excess density of the partially molten zone (~40 kg m^{-3}), ΔV is its volume (~20% of the mantle volume), d is the height of the partially molten zone from the core–mantle boundary (~2,000 km), ρ is the density of the partially molten zone (~4,500 kg m^{-3}), and C_p is the specific heat (~1,200 J kg^{-1} K^{-1}). The temperature increase by the release of gravitational potential energy is limited to ~170 K, which is a small fraction of the temperature difference between the solidus and the mantle adiabat corresponding to the partially molten zone [~1,000 K for the adiabat with the potential temperature of 1,750 K (53)].

Oxidation of Metal Droplets. A metallic component of an impactor can efficiently react with silicate melt when it is fragmented to millimeter- to centimeter-scale droplets (54). Possible redox reactions in a magma ocean include

$$Fe_2O_3 + Fe \rightarrow 3FeO, \quad [7]$$

$$H_2O + Fe \rightarrow H_2 + FeO. \quad [8]$$

If a metal droplet is entirely consumed by the above reactions, HSEs contained in the droplet would be transferred to the silicate mantle.

An order-of-magnitude calculation suggests that this oxidation-based metal retention does not consume all of the relevant metal droplets, the collective mass of which is assumed here to be 10^{22} kg for the sake of discussion. Assuming that a large late-accretion impactor melts the entire upper mantle (~10^{24} kg) with 8 wt% FeO (55) and that the mantle is already as oxidized as the present-day mantle [$Fe^{3+}/Fe^T \sim 0.04$ (56)], the amount of Fe^{3+} in a local magma ocean would be 2.5×10^{21} kg or 4.4×10^{22} mol. This could potentially reduce 25% of 10^{22} kg of Fe (or 1.8×10^{23} mol of Fe). Similarly, assuming that the mantle contains one-ocean-worth water (1.4×10^{21} kg H_2O), a molten upper mantle would have 1.9×10^{22} mol of H_2O, which could reduce only ~4% of 10^{22} kg of Fe.

Furthermore, because a local magma ocean becomes metal-saturated after these oxidation reactions, the oxygen fugacity of silicate melt is controlled by the iron–wüstite (IW) buffer, which dictates the ratio of ferric iron over total iron. Because the effective pressure of chemical reaction between the metallic phase and the silicate melt phase is somewhere in the middle of a magma ocean (57), and because the IW buffer under high pressures and high temperatures results in a high Fe^{3+}/Fe^T [~0.1; (58)], chemical reactions between metal droplets and silicate melt likely increase the bulk Fe^{3+}/Fe^T of a local magma ocean. This means that the reaction of Eq. **7** is actually reversed, preventing the assimilation of HSEs in the silicate mantle. From these considerations, the oxidative metal retention in a magma ocean is likely to be limited.

Modeling of Three-phase Flow. The percolation of liquid metal into a partially molten zone involves three phases, i.e., solid silicate, molten silicate, and liquid metal. Because the timescale of our interest is very short (days to years; see Rayleigh-Taylor instability of a metal layer), the deformation of solid silicate is negligible, and we can focus on the dynamics of two fluid phases, the wetting fluid (molten silicate) and the nonwetting fluid (liquid metal) (59). In this case, the mass balance equations are

$$\frac{\partial}{\partial t}(\phi S_w \rho_w) = -\nabla \cdot (\rho_w \mathbf{q}_w), \quad [9]$$

$$\frac{\partial}{\partial t}(\phi S_n \rho_n) = -\nabla \cdot (\rho_n \mathbf{q}_n), \quad [10]$$

where ϕ is porosity, ρ is density, S is saturation, and $\mathbf{q}$ is specific discharge (or flux), and the subscripts "w" and "n" denote the wetting and nonwetting fluids, respectively. The momentum balance equations are

$$\mathbf{q}_w = -\frac{\mathbf{k}_w(S_w)}{\mu_w}\left(\nabla p_w + \rho_w g \nabla z\right), \quad [11]$$

$$\mathbf{q}_n = -\frac{\mathbf{k}_n(S_n)}{\mu_n}\left(\nabla p_n + \rho_n g \nabla z\right), \quad [12]$$

where $\mathbf{k}$ is effective permeability, p is pressure, and $-g\nabla z$ denotes the body force due to gravity.

Assuming an isotropic porosity, effective permeabilities are defined through relative permeabilities, k_r, as

$$k_w(S_w) = k_{\text{sat}} k_{rw}(S_w), \quad [13]$$

$$k_n(S_n) = k_{\text{sat}} k_{rn}(S_n), \quad [14]$$

where k_{sat} is the permeability at full saturation and is a function of porosity as well as grain size, d, as

$$k_{\text{sat}}(\phi) = \frac{d^2}{150}\frac{\phi^3}{(1-\phi)^2}, \quad [15]$$

which is the so-called Blake–Kozeny equation (60). The relative permeabilities are calculated as

$$k_r(S) = \frac{S - S_{\min}}{1 - S_{\min}}, \quad [16]$$

with a minimum value of 10^{-3}. Based on the dihedral angles of molten silicate and liquid metal in partially molten silicate aggregates (61, 62), $S_{\min}$ is set to 0.01 for the wetting fluid and 0.2 for the nonwetting fluid. The pressure for the wetting fluid may be decomposed to the lithostatic pressure, $\rho_m g z$, where ρ_m is the density of the solid mantle, and the dynamic pressure, δp. The pressures for the wetting and nonwetting fluids are connected through the capillary pressure, p_c, as

$$p_c(S_w) = p_n - p_w, \quad [17]$$

and the magnitude of the capillary pressure is bounded as

$$p_c \le p_{c,\max} = \frac{2\gamma_{wn}}{r_{\min}}, \quad [18]$$

where γ_{wn} is the interface tension between the wetting and nonwetting fluids and $r_{\min}$ is the minimum radius of curvature of the microscopic interface between these fluids. The work of ref. 62 suggests $\gamma_{wn} \sim 0.5$ J m^{-2}, so using the grain size of 1 mm for $r_{\min}$, the maximum capillary pressure is $\sim 10^3$ Pa. In our modeling, $S_n \ll 1$, so p_c is set to this maximum value for simplicity. Finally, there is a saturation balance as

$$S_w + S_n = 1. \quad [19]$$

Eqs. **9**–**19** are solved by an upwind finite-difference scheme for one-dimensional flow, subject to the following initial and boundary conditions:

$$\phi(z) = 0.4(1 - z/z_{\max}), \quad [20]$$

$$S_w(z, 0) = 1, \quad [21]$$

$$S_w(0, t) = 0, \quad [22]$$

$$S_n(z, 0) = 0, \quad [23]$$

$$S_n(0, t) = 1, \quad [24]$$

where $z_{\max}$ is the depth of a partially molten zone. The vertical grid interval is set to 1 km, and a time step of 36 s is used. The following material properties are used: $\rho_m = 3{,}300$ kg m^{-3}, $\rho_w = 3{,}000$ kg m^{-3}, $\rho_m = 7{,}500$ kg m^{-3}, $\mu_w = 10$ Pa s, and $\mu_n = 10^{-3}$ Pa s. Some representative solutions are shown in *SI Appendix*, Fig. S2. The metal concentration takes its maximum at $z = 0$ and gradually decreases downward almost linearly.

Modeling of Subsolidus Mantle Convection. To model convective mixing by subsolidus mantle convection, we solve the nondimensionalized governing equations for thermal convection of an incompressible fluid, consisting of the conservation of mass,

$$\nabla \cdot \mathbf{u}^* = 0, \quad [25]$$

the conservation of momentum,

$$-\nabla P^* + \nabla \cdot [\eta^*(\nabla \mathbf{u}^* + \nabla \mathbf{u}^{*T})] + Ra T^* \mathbf{e}_z = 0, \quad [26]$$

and the conservation of energy,

$$\frac{\partial T^*}{\partial t^*} + \mathbf{u}^* \cdot \nabla T^* = \nabla^2 T^* + H^*. \quad [27]$$

The unit vector pointing upward is denoted by $\mathbf{e}_z$. Asterisks denote nondimensional variables. The spatial coordinates are normalized by the mantle depth D(= 2,900 km), and time is normalized by the diffusion time scale, D^2/κ, where κ is thermal diffusivity (= 10^{-6} m^2 s^{-1}). Velocity $\mathbf{u}^*$ is thus normalized by κ/D. Dynamic pressure P^* and viscosity η^* are normalized by $\eta_0\kappa/D^2$ and η_0, respectively, where η_0 is a reference viscosity at $T^* = 1$. Temperature T^* is normalized by a potential temperature difference between the surface and the core–mantle boundary, ΔT (= 2,000 K). The Rayleigh number Ra is defined here as

$$Ra = \frac{\alpha \rho_0 g \Delta T D^3}{\kappa \eta_0}, \quad [28]$$

where α is thermal expansivity (= 10^{-5} K^{-1}), ρ_0 is reference density (= 5,000 kg m^{-3}), and g is gravitational acceleration. These values for thermal expansivity and reference density are appropriate for the lowermost mantle, and this is because the competition between thermal and chemical buoyancies near the core–mantle boundary region determines the efficiency of convective entrainment of dense metal-impregnated components. We tested two reference viscosities, 2.39×10^{21} Pa s and 7.97×10^{20} Pa s, to have Ra of 10^7 and 3×10^7, respectively. These viscosities are higher than mantle viscosity appropriate for the Hadean, as we are concerned with the long-term effect of mantle mixing through Earth history. Heat generation H^* is defined as

$$H^* = \frac{\rho_0 H D^2}{k \Delta T}, \quad [29]$$

where H is heat production rate per unit mass and k is thermal conductivity. We tested a few values of H^* to achieve an Earth-like internal heating rate (~0.6 to 0.7), which includes the effect of secular cooling (63). Viscosity is both temperature- and depth-dependent. The temperature dependence is prescribed by

$$\eta_T^* = \exp[\theta(1 - T^*)], \quad [30]$$

where θ is called the Frank–Kamenetskii parameter, and reference viscosity for the bottom three quarters of the mantle is raised by a factor of 30 (64).

The above governing equations are solved with the two-dimensional finite element code of ref. 65. The top and bottom boundaries are free slip. The top and bottom (nondimensional) temperatures are set to 0 and 1, respectively. A reflecting (i.e., free slip and insulating) boundary condition is applied to the side boundaries. The aspect ratio of a model is four to reduce wall effects, and the model is discretized by 400 × 100 uniform quadrilateral elements. Internal temperature is set to 0.7 at $t^* = 0$ with random perturbations of small amplitude (10^{-3}), and the system is integrated until $t^* = 0.0169$, which corresponds to 4.5 billion years.

The chemical composition is tracked by 10^8 tracers, which are initially randomly distributed and are advected with a fourth-order Runge–Kutta scheme (66). A certain fraction of these tracers are associated with a density anomaly of 4,000 kg m^{-3} to represent metallic components. For a total metal mass of 10^{22} kg, for example, 0.25% of the tracers (2.5×10^5 tracers) are marked as dense tracers. Based on the results of three-phase flow modeling, such dense tracers are then distributed at mid-mantle depths, corresponding to the location of a hypothetical partially molten zone (Fig. 3 *A* and *B*). With a total metal mass of 10^{22} kg, a laterally homogeneous, 750-km-thick partially molten zone

would have an average metal concentration of ∼0.97%, and because metal concentration is expected to vary linearly within the zone (*SI Appendix*, Fig. S2), dense tracers are distributed so that the concentration is ∼1.93% at the top of the zone and linearly decreases to zero at its bottom. This would correspond to the case of a 3% Earth mass impactor with an impact angle of 45° and v/v_e=2.2 (*SI Appendix*, Table S3). We tested seven different initial tracer distributions. Four of them are with laterally homogeneous partially molten zones, all with the total metal mass of 10^{22} kg, the complete mixing of which would reproduce the present-day mantle abundance of HSEs. The thickness of the zone is 250 km (Case 1), 500 km (Case 2), 750 km (Case 3), and 1,000 km (Case 4). The rest of the cases all have a 1,000-km-thick partially molten zone with a locally deep, 500-km-thick partially molten zone for the mid-50% of the lateral extent. The total amount of metal in the deep zone is the same as that in the shallow zone in Case 5, and it is greater by 25% in Case 6 and 50% in Case 7. Thus, the total metal mass is 1.13×10^{22} kg in Case 6 and 1.25×10^{22} kg in Case 7.

For each of these seven initial tracer distributions, we have tested two Rayleigh numbers (10^7 and 3×10^7), two internal heat production (20 and 25 for $Ra = 10^7$, and 25 and 30 for $Ra = 3 \times 10^7$), and three Frank-Kamenetskii parameters (4.61, 5.70, and 6.91, which corresponds to the total viscosity contrast due to temperature of 10^2, 3×10^2, and 10^3, respectively), amounting to a total of 84 model runs. Convection and mixing diagnostics are summarized in *SI Appendix*, Fig. S3. In general, greater temperature dependence of viscosity brings the system closer to stagnant lid convection, thereby decreasing the mixing efficiency (*SI Appendix*, Fig. S3 *A–C*) as well as the surface heat flux (*SI Appendix*, Fig. S3 *G–I*). The internal heating ratio is high when mixing is inefficient (i.e., low metal concentration in the present-day upper mantle) (*SI Appendix*, Fig. S3 *D–F*), because dense metal-impregnated components occupy a large fraction of the core–mantle boundary, reducing the core heat flux.

Our convection modeling is certainly simplified in a few important ways, such as the use of a two-dimensional Cartesian box and time-invariant internal heating, but what matters for the efficient convective entrainment of dense materials is the strength of upwelling currents in the lowermost mantle. We have tested a wide range of relevant model parameters, and this exploration of the model space is deemed sufficient to support our main conclusions.

On the Possibility of Metal Percolation through the Core–Mantle Boundary Region. A recent experimental study suggests the possibility of interconnected liquid metal in a stressed bridgmanite matrix (67), so liquid metal in the metal-impregnated mantle components above the core–mantle boundary may further drain down to the core. However, the percolative potential of liquid metal is unlikely to be as important as suggested for the following reasons. First, their experiments were conducted with the metal fraction of 5%, which is greater than the theoretical threshold fraction (3%) for percolation under a hydrostatic condition [Note: Metal fraction in the metal-impregnated mantle components in our model is generally lower than this (Fig. 4 *C–F*)]. Even with this relatively high fraction, melt pockets were not interconnected in their hydrostatic experiments, and this discrepancy is attributed to the possibility that metal is not perfectly distributed in the system. With shearing, they observed the formation of an interconnected metal network, but because the metal fraction is already above the threshold fraction for a hydrostatic condition, it is difficult to extract the effect of shear stress from their experiments. Second, the maximum strain achieved in their experiments is still quite low (<1), and the stability of the interconnected metal network remains uncertain. In fact, with continuing deformation, elongated and thinned network channels are expected to be disintegrated into small isolated pockets (68), and this process likely continues until the radius of such isolated pockets becomes small enough to achieve a balance between shear stress and interfacial energy divided by the radius. We note that the proposed metal percolation mechanism (67) is much less efficient than the Rayleigh–Taylor instability (i.e., diapir formation; see the above subsection on time scale estimates), and it is unlikely to contribute to metal removal from the mantle.

Data, Materials, and Software Availability. The summary of postprocessing of SPH simulations is reported in *SI Appendix*. Raw numerical data required to reproduce figures have been deposited in Mendeley Data (69). All study data are included in the article and/or *SI Appendix*.

ACKNOWLEDGMENTS. We thank Norm Sleep, John Hernlund, and an anonymous reviewer for constructive comments and Rich Walker and Alessandro Morbidelli for discussion. This research was supported in part by the US NSF EAR-2102777 and the US NASA under Cooperative Agreement No. 80NSSC19M0069 issued through the Science Mission Directorate.

1. C.-L. Chou, "Fractionation of siderophile elements in the Earth's upper mantle" in *Proceedings of the 9th Lunar and Planetary Science Conference* (1978), pp. 219–230.
2. K. Kimura, R. S. Lewis, E. Anders, Distribution of gold and rhenium between nickel–iron and silicate melts: Implications for the abundance of siderophile elements on the Earth and Moon. *Geochim. Cosmochim. Acta* **38**, 683–701 (1978).
3. R. J. Walker, Highly siderophile elements in the Earth, Moon and Mars: Update and implications for planetary accretion and differentiation. *Chem. Erde* **69**, 101–125 (2009).
4. J. M. D. Day, A. D. Brandon, R. J. Walker, Highly siderophile elements in Earth, Mars, the Moon, and asteroids. *Rev. Mineral. Geochem.* **81**, 161–238 (2016).
5. S. Marchi, R. M. Canup, R. J. Walker, Heterogeneous delivery of silicate and metal to the Earth by large planetesimals. *Nat. Geosci.* **11**, 77–81 (2018).
6. W. Neumann, T. S. Kruijer, D. Breuer, T. Kleine, Multistage core formation in planetesimals revealed by numerical modeling and Hf-W chronometry of iron meteorites. *J. Geophys. Res. Planets* **123**, 421–444 (2018).
7. R. I. Citron, S. T. Stewart, Large impacts onto the early Earth: Planetary sterilization and iron delivery. *Planet. Sci. J.* **3**, 116 (2022).
8. H. Genda, R. Brasser, S. J. Mojzsis, The terrestrial late veneer from core disruption of a lunar-sized impactor. *Earth Planet. Sci. Lett.* **480**, 25–32 (2017).
9. R. Deguen, M. Landeau, P. Olson, Turbulent metal-silicate mixing, fragmentation, and equilibration in magma oceans. *Earth Planet. Sci. Lett.* **391**, 274–287 (2014).
10. M. Landeau *et al.*, Melta-silicate mixing by large Earth-forming impacts. *Earth Planet. Sci. Lett.* **564**, 116888 (2021).
11. H. J. Melosh, A. M. Vickery, Melt droplet formation in energetic impact events. *Nature* **350**, 494–497 (1991).
12. G. Lavorel, M. Le Bars, Sedimentation of particles in a vigorously convecting fluid. *Phys. Rev. E* **80**, 046324 (2009).
13. G. Fiquet *et al.*, Melting of peridotite to 140 gigapascals. *Science* **329**, 1516–1518 (2010).
14. Y. Miyazaki, J. Korenaga, On the timescale of magma ocean solidification and its chemical consequences: 2. Compositional differentiation under crystal accumulation and matrix compaction. *J. Geophys. Res. Solid Earth* **124**, 3399–3419 (2019).
15. H. G. Ave Lallemant, J.-C. C. Mercier, N. L. Carter, J. V. Ross, Rheology of the upper mantle: Inferences from peridotite xenoliths. *Tectonophysics* **70**, 85–113 (1980).
16. V. S. Solomatov, C. C. Reese, Grain size variations in the Earth's mantle and the evolution of primordial chemical heterogeneities. *J. Geophys. Res.* **113**, B07408 (2008).
17. A. M. Forte, N. A. Simmons, S. P. Grand, "Constraints on seismic models from other disciplines–Constraints on 3-D seismic models from global geodynamic observables: Implications for the global mantle convective flow" in *Treatise on Geophysics* (Elsevier, ed. 2, 2015), vol. 1, pp. 853–907.
18. C. Jain, J. Korenaga, Synergy of experimental rock mechanics, seismology, and geodynamics reveals still elusive upper mantle rheology. *J. Geophys. Res. Solid Earth* **125**, e2020JB019896 (2020).
19. V. Lekic, S. Cottaar, A. Dziewonski, B. Romanowicz, Cluster analysis of global lower mantle tomography: A new class of structure and implications for chemical heterogeneity. *Earth Planet. Sci. Lett.* **357–358**, 68–77 (2012).
20. E. J. Garnero, A. K. McNamara, S.-H. Shim, Continent-sized anomalous zones with low seismic velocity at the base of Earth's mantle. *Nat. Geosci.* **9**, 481–488 (2016).
21. I. N. Tolstikhin, J. D. Kramers, A. W. Hofmann, A chemical Earth model with whole mantle convection: The importance of a core-mantle boundary layer (D") and its early formation. *Chem. Geol.* **226**, 79–99 (2006).
22. C.-T.A. Lee *et al.*, Upside-down differentiation and generation of a 'primordial' lower mantle. *Nature* **463**, 930–933 (2010).
23. R. W. Carlson *et al.*, How did early Earth become our modern world? *Annu. Rev. Earth Planet. Sci.* **42**, 151–178 (2014).
24. H. Deng *et al.*, Primordial Earth mantle heterogeneity caused by the Moon-forming giant impact? *Astrophys. J.* **887**, 211 (2019).
25. Q. Yuan, M. M. Li, S. J. Desch, B. Ko, "Giant impact origin for the large low shear velocity provinces" in *52nd Lunar and Planetary Science Conference 2021* (2021), p. 1980.
26. S. Cottaar, V. Lekic, Morphology of seismically slow lower-mantle structures. *Geophys. J. Int.* **207**, 1122–1136 (2016).
27. M. Ishii, J. Tromp, Normal-mode and free-air gravity constraints on lateral variations in velocity and density of Earth's mantle. *Science* **285**, 1231–1236 (1999).
28. H. C. P. Lau *et al.*, Tidal tomography constrains Earth's deep-mantle buoyancy. *Nature* **551**, 321–325 (2017).
29. A. K. McNamara, A review of large low shear velocity provinces and ultra low velocity zones. *Tectonophysics* **760**, 199–220 (2019).
30. W. D. Maier *et al.*, Progressive mixing of meteoritic veneer into the early Earth's deep mantle. *Nature* **460**, 620–623 (2009).

31. I. S. Puchtel, J. Blichert-Toft, M. Touboul, R. J. Walker, ^{182}W and HSE constraints from 2.7 Ga komatiites on the heterogeneous nature of the Archean mantle. *Geochim. Cosmochim. Acta* **228**, 1–26 (2018).
32. J. R. Reimink *et al*., Tungsten isotope composition of Archean crustal reservoirs and implications for terrestrial μ^{182}W evolution. *Geochem. Geophys. Geosyst.* **21**, e2020GC009155 (2020).
33. W. F. McDonough, "Compositional model for the Earth's core" in *Treatise on Geochemistry*, H. D. Holland, K. K. Turekian, Eds. (Elsevier, 2003), vol. 2, pp. 547–568.
34. T. Lyubetskaya, J. Korenaga, Chemical composition of Earth's primitive mantle and its variance, 1, methods and results. *J. Geophys. Res.* **112**, B03211 (2007).
35. A. Mundl-Petermeier *et al*., Anomalous ^{182}W in high ^{3}He^{4}He ocean island basalts: Fingerprints of Earth's core? *Geochim. Cosmochim. Acta* **271**, 194–211 (2020).
36. G. J. Archer *et al*., Lack of late-accreted material as the origin of ^{182}W excesses in the Archean mantle: Evidence from the Pilbara Craton, Western Australia. *Earth Planet. Sci. Lett.* **528**, 115841 (2019).
37. T. Yoshino, Y. Makino, T. Suzuki, T. Hirata, Grain boundary diffusion of W in lower mantle phase with implications for isotopic heterogeneity in oceanic island basalts by core–mantle interactions. *Earth Planet. Sci. Lett.* **530**, 115887 (2020).
38. A. L. Ferrick, J. Korenaga, Long-term core-mantle interaction explains W-He isotope heterogeneities. *Proc. Nat. Acad. Sci. U.S.A.* **120**, e2215903120 (2023).
39. A. Mundl-Petermeier *et al*., Temporal evolution of primordial tungsten-182 and ^{3}He/^{4}He signatures in the Iceland mantle plume. *Chem. Geol.* **525**, 245–259 (2019).
40. M. Nakajima, D. J. Stevenson, Melting and mixing states of the Earth's mantle after the Moon-forming impact. *Earth Planet. Sci. Lett.* **427**, 286–295 (2015).
41. H. E. Newsom an S. R. Taylor., Geochemical implications of the formation of the Moon by a single giant impact. *Nature* **338**, 29–34 (1989).
42. N. H. Sleep, Asteroid bombardment and the core of Theia as possible sources for the Earth's late veneer component. *Geochem. Geophys. Geosyst.* **17**, 2623–2642 (2016).
43. J. Zhang, C. Herzberg, Melting experiments on anhydrous peridotite KLB-1 from 5.0 to 22.5 GPa. *J. Geophys. Res.* **99**, 17729–17742 (1994).
44. Y. Miyazaki, J. Korenaga, On the timescale of magma ocean solidification and its chemical consequences: 1. Thermodynamic database for liquid at high pressures. *J. Geophys. Res. Solid Earth* **124**, 3382–3398 (2019).
45. Y. Abe, "Thermal evolution and chemical differentiation of the terrestrial magma ocean" in *Evolution of the Earth and Planets*, E. Takahashi, R. Jeanloz, R. Rudie, Eds. (AGU, Washington, D.C., 1993), pp. 41–54.
46. V. Solomatov, "Magma oceans and primordial mantle differentiation" in *Treatise on Geophysics* (Elsevier, ed. 2, 2015), vol. 9, pp. 81–104.
47. D. Defays, An efficient algorithm for a complete link method. *Comput. J.* **20**, 364–366 (1977).
48. D. L. Turcotte, G. Schubert, *Geodynamics: Applications of Continuum Physics to Geological Problems* (John Wiley, New York, NY, 1982).
49. Y. Miyazaki, J. Korenaga, A wet heterogeneous mantle creates a habitable world in the Hadean. *Nature* **603**, 86–90 (2022).
50. P. Mondal, J. Korenaga, The Rayleigh-Taylor instability in a self-gravitating two-layer viscous sphere. *Geophys. J. Int.* **212**, 1859–1867 (2018).
51. E. Stolper, D. Walker, B. H. Hager, J. F. Hays, Melt segregation from partially molten source regions: The importance of melt density and source region size. *J. Geophys. Res.* **86**, 6261–6271 (1981).
52. J. A. Whitehead, D. S. Luther, Dynamics of laboratory diapir and plume models. *J. Geophys. Res.* **80**, 705–717 (1975).
53. J. Korenaga, Rapid solidification of Earth's magma ocean limits early lunar recession. *Icarus* **400**, 115564 (2023).
54. D. C. Rubie, H. J. Melosh, J. E. Reid, C. Liebske, K. Righter, Mechanisms of metal-silicate equilibration in the terrestrial magma ocean. *Earth Planet. Sci. Lett.* **205**, 239–255 (2003).
55. W. F. McDonough, S.-S. Sun, The composition of the Earth. *Chem. Geol.* **120**, 223–253 (1995).
56. P. A. Sossi *et al*., Redox state of Earth's magma ocean and its Venus-like early atmosphere. *Sci. Adv.* **6**, eabd1387 (2020).
57. R. A. Fischer *et al*., High pressure metal-silicate partitioning of Ni Co, V, Cr, Si, and O. *Geochim. Cosmochim. Acta* **167**, 177–194 (2015).
58. J. Deng, Z. Du, B. B. Karki, D. B. Ghosh, K. K. M. Lee, A magma ocean origin to divergent redox evolutions of rocky planetary bodies and early atmospheres. *Nat. Commun.* **11**, 2007 (2020).
59. J. Bear, *Modeling Phenomena of Flow and Transport in Porous Media* (Springer, 2018).
60. F. A. L. Dullien, *Porous Media: Fluid Transport and Pore Structure* (Academic Press, New York, NY, 1979).
61. M. J. Daines, F. M. Richter, An experimental method for directly determining the interconnectivity of melt in a partially molten system. *Geophys. Res. Lett.* **15**, 1459–1462 (1988).
62. A. Holzheid, M. D. Schmitz, T. L. Grove, Textural equilibria of iron sulfide liquids in partly molten silicate aggregatres and their relavance to core formation scenarios. *J. Geophys. Res.* **105**, 13555–13567 (2000).
63. J. Korenaga, Pitfalls in modeling mantle convection with internal heating. *J. Geophys. Res. Solid Earth* **122**, 4064–4085 (2017).
64. B. H. Hager, Subducted slabs and the geoid: Constraints on mantle rheology and flow. *J. Geophys. Res.* **89**, 6003–6015 (1984).
65. J. Korenaga, T. H. Jordan, Physics of multiscale convection in Earth's mantle: Onset of sublithospheric convection. *J. Geophys. Res.* **108**, 2333 (2003).
66. U. R. Christensen, D. A. Yuen, The interaction of a subducting lithospheric slab with a chemical or phase boundary. *J. Geophys. Res.* **89**, 4389–4402 (1984).
67. L. Wang, Y. Fei, A partially equilibrated initial mantle and core indicated by stress-induced percolative core formation through a bridgmanite matrix. *Sci. Adv.* **9**, eade3010 (2023).
68. N. Groebner, D. L. Kohlstedt, Deformation-induced metal melt networks in silicates: Implications for core–mantle interactions in planetary bodies. *Earth Planet. Sci. Lett.* **245**, 571–580 (2006).
69. J. Korenaga, S. Marchi, Numerical data for the figures of Korenaga & Marchi (2023). Mendeley Data. https://doi.org/10.17632/dhhgdf2krb.1. Deposited 13 September 2023.